

Experimental observation and theoretical analysis of Raman resonance-enhanced photodamage in coherent anti-Stokes Raman scattering microscopy

Haifeng Wang and Yan Fu

Weldon School of Biomedical Engineering, Purdue University, West Lafayette, Indiana 47907, USA

Ji-Xin Cheng

Weldon School of Biomedical Engineering and Department of Chemistry, Purdue University, West Lafayette, Indiana 47907, USA

Received May 12, 2006; revised October 6, 2006; accepted October 24, 2006;
posted October 27, 2006 (Doc. ID 70864); published February 15, 2007

The photodamage in coherent anti-Stokes Raman scattering (CARS) imaging of spinal tissues is featured by plasma-induced myelin splitting and shockwaves. When the excitation is tuned on resonance with the symmetric CH_2 stretch vibration, the average point-scanning time to cause the photodamage is reduced by half. Similar Raman resonance-enhanced photodamage is also observed for a polymer film. The light-matter energy transfer in coherent Raman processes with both plane waves and focused excitation beams is analyzed to interpret this phenomenon. Our calculation indicates that at Raman resonance, a significant vibrational absorption in the material can be stimulated by the concomitant Raman gain and Raman loss processes due to high incident-field intensities under a tight-focusing condition. As a result, while the nonlinear damage induced by multiphoton absorption can be diminished in CARS microscopy owing to the use of near-infrared picosecond pulses, the coherent Raman-induced vibrational pumping is able to enhance the photodamage by assisting plasma generation in the material. © 2007 Optical Society of America

OCIS codes: 180.5810, 190.5650, 260.2160.

1. INTRODUCTION

Coherent anti-Stokes Raman scattering (CARS) microscopy¹⁻³ is an exciting tool for high-sensitivity three-dimensional vibrational imaging of lipid bilayers,⁹⁻¹¹ myelin sheath,¹² lipid bodies,^{13,14} and drug molecules.¹⁵ Owing to the use of tightly focused ultrafast laser beams, photodamage is a significant issue in multiphoton microscopy.¹⁶⁻¹⁸ In a recent paper, we have systematically studied the photodamage in CARS imaging of intact myelin sheath in spinal tissues and cultured cells.¹⁹ We showed that the myelin was torn apart by absorption-generated plasma at the laser foci. Interestingly, the photodamage rate was increased when the excitation was tuned on resonance to CH_2 vibration.¹⁹ Additionally, we have also observed Raman resonance-enhanced photodamage in a polymer film sample, which will be reported in this paper.

In this paper, we present a mechanistic study of Raman resonance-enhanced photodamage through a theoretical analysis of light-matter energy transfer in CARS microscopy. CARS is a four-wave mixing process in which the interaction of a pump field E_1 at frequency ω_1 and a Stokes field E_2 at frequency ω_2 with a material generates a coherent Raman signal at the anti-Stokes frequency ω_{as}

$= 2\omega_1 - \omega_2$.²⁰⁻²² The CARS field E_{as} is related to the material and the incident fields by $E_{as} \propto \chi^{(3)} E_1 E_2^* E_1$, where $\chi^{(3)}$ is the third-order nonlinear susceptibility. In a CARS experiment, various coherent Raman processes occur simultaneously, including CARS, coherent Stokes Raman scattering (CSRS), stimulated Raman gain (SRG), stimulated Raman loss (SRL), and Raman-induced Kerr effect (RIKE).²²⁻²⁶ In CSRS, a new field E_s at the Stokes frequency $\omega_s = 2\omega_2 - \omega_1$ is generated. In SRG, the ω_2 field experiences a gain, while in SRL the ω_1 field experiences a loss. In RIKE, new polarization components of the excitation fields are generated. In most CARS imaging experiments, two parallel-polarized beams are used, where RIKE is negligible ($\chi_{2111} = 0$ for isotropic medium).^{27,28} In CARS and CSRS, the nonlinear polarization generates the signal at new frequencies, whereas the signal in SRG and SRL is coherently mixed with the excitation beams. Owing to the heterodyne nature of SRG and SRL, the light-matter energy transfer in these two processes is much bigger than that in CARS and CSRS. The efficiencies of light-matter energy transfer induced by SRG and SRL under our experimental conditions are calculated. Our results show that with tightly focused laser beams,

RG and SRL at Raman resonance can transfer approximately 0.02% energy to the material through vibrational excitation in a small focal volume. This vibrational pumping could contribute to plasma generation and enhance the photodamage accordingly.

2. EXPERIMENTAL OBSERVATION

We first describe our observation of Raman resonance-induced photodamage to myelin sheath. The tissue sample preparation and the CARS microscope setup were described elsewhere.¹² Briefly, two synchronized Ti:sapphire lasers (Mira 900, Coherent Inc.) were used to generate the pump and Stokes excitation beams. The output pulse duration was around 2.5 ps. The spectral FWHM (full width at half-maximum) was 0.4 nm as measured with a spectrometer (HR2000, Ocean Optics). A Pockels cell was used to reduce the pulse repetition rate from 77 MHz to a few megahertz. The two laser beams were collinearly combined and directed into a laser-scanning confocal microscope (IX70/FV300, Olympus Inc). A 60 \times water-immersion objective with a numerical aperture (N.A.) of 1.2 was used to focus the laser beams into the sample. The epi-detected-CARS (E-CARS) signal was collected by the same water objective and probed with an external photomultiplier tube (PMT) detector installed at the microscope back port. The forward-CARS (F-CARS) signal was collected by an air condenser (N.A. = 0.55) and probed with another external PMT. E-CARS was used for the thick spinal tissues for which F-CARS detection is inefficient owing to sample scattering.

Figure 1 shows our observation of photodamage in myelin sheath. The CARS image of a single myelinated axon is shown in Fig. 1(a). Here $\omega_1 - \omega_2$ was tuned to 2840 cm^{-1} , in resonance with the symmetric CH_2 stretch vibration. The myelin sheath, which contains 70% lipid and 30% protein in weight,²⁹ produces a strong resonant CARS signal. To analyze the photodamage mechanism, we intentionally induced myelin damage by using the point-scan mode. In this mode the laser beams were focused at a fixed position on the sample (myelin sheath in our case) during the scanning. Initially the CARS signal from the myelin sheath was large and constant, indicating no damage. After a certain time (usually several seconds), the photodamage occurred, characterized by tearing off of the myelin sheath as shown in Fig. 1(b). This damage was probably caused by plasma generation induced by absorption, as pointed out by our recent paper.¹⁹ The generated plasma can strongly absorb laser energy, expand, and disrupt the tissue mechanically.^{18,30,31} As a result the damaged area in Fig. 1(b) was larger than the focal volume. Meanwhile, the CARS signal at the damaged site dropped suddenly, as shown in a typical CARS signal trace taken during the point scan [Fig. 1(c)]. We have repeated this damaging process in different spinal tissue samples. The average scanning time to cause photodamage, referred to as “photodamage time” in the rest of the paper, is used to quantify the photodamage rate. We have observed that the photodamage rate depends strongly on the pulse peak power, indicating the nonlinear nature of the observed myelin damage.¹⁹

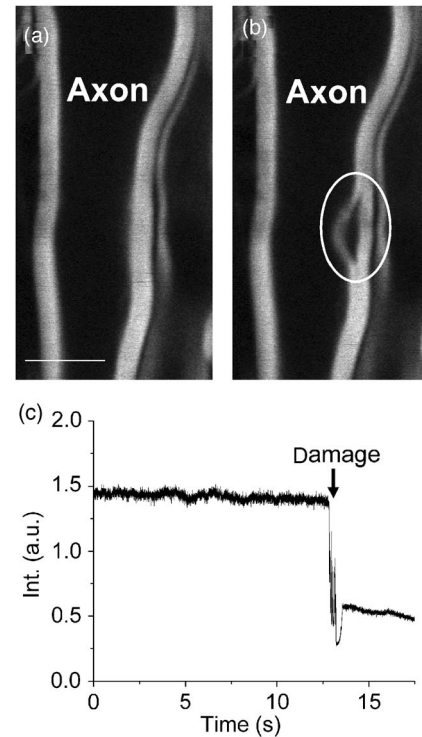


Fig. 1. Photodamage induced in CARS imaging of myelin sheath. (a) CARS image of a nondamaged myelinated axon. Laser repetition rate, 7.8 MHz; average pump beam power, 6.48 mW; average Stokes beam power, 2.52 mW. The corresponding peak power is 415 and 108 W for the pump and Stokes beams, respectively. Bar = 5 μm . (b) CARS image of the same axon after photodamage induced by point scanning. The damage tears apart the myelin at the laser focus (circled area), (c) Typical point-scan trace. The CARS signal drops when photodamage happens. Int., intensity.

To inspect whether Raman resonance enhances the photodamage, we have measured the time to cause photodamage at various Raman shifts. We fixed the wavelength of the pump beam at 703 nm (14,225 cm^{-1}) and tuned the Stokes beam in the region of 860 to 891 nm to generate the Raman shift in the range from 2600 and 3000 cm^{-1} . According to the CARS spectrum of single-axonal myelin [Fig. 2(a)], 2840 cm^{-1} is the resonant peak with the symmetric CH_2 stretch vibration. Note that Fig. 2(a) was produced using the image-acquisition mode, and no damage was observed at the acquisition rate of 1 frame/s. For all the photodamage experiments, the pump and Stokes laser power at the sample were 1.1 and 0.66 mW, respectively. The repetition rate of both lasers was 1.3 MHz. Thus, the pump and Stokes pulse energies were 0.85 and 0.51 nJ, respectively. We realize that the photodamage time is sensitive to the pulse duration, the spatial and temporal overlap between the pump and the Stokes beams, the size of the focus, and the local molecular density at the focus. To get the best data repeatability as we can, we have done the following, besides keeping constant laser powers: (1) The Stokes pulse duration was monitored by an autocorrelator and kept constant at 2.5 ps during tuning. (2) The CARS signal was optimized to ensure the best temporal overlap between the pump and the Stokes pulses. (3) For our beam-scanning microscope, the spatial overlap between the pump and the Stokes beams

is the best at the center of the field of view; therefore we always moved the target myelin to the center of the field of view so that the point scanning can be performed with optimal spatial overlap of the two beams. Additionally, we chose only myelin sheath within a $50\text{ }\mu\text{m}$ penetration depth, which minimized beam distortion during propagation inside the tissue. (4) We tuned the z position of the objective to ensure that the laser focus was on the equatorial plane of the target myelin, where the myelin shows the clearest edge and highest CARS signal. To have constant molecular density at the focus, myelin with similar diameter and CARS signal was used for the measurement of the photodamage time. (5) Because the second instance of photodamage on the same myelin was found much faster, we have avoided repeated photodamage on the myelin of the same axon.

The experimental results for the photodamage of myelin sheath are shown in Fig. 2(b). The average point-scan time to cause photodamage was $0.86\pm 0.32\text{ s}$ at 2840 cm^{-1} and $0.81\pm 0.10\text{ s}$ at 2860 cm^{-1} , while for the other Raman shifts a longer average time was needed. For the Raman shifts at 2600 and 3000 cm^{-1} , which were far away from resonance, an average time of $1.54\pm 0.45\text{ s}$ and $1.53\pm 0.32\text{ s}$ was needed, respectively. The photodamage at off-resonance frequencies was probably induced by two-

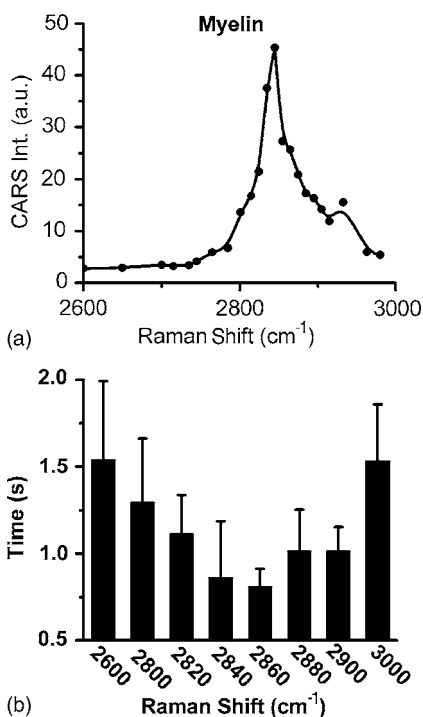


Fig. 2. Raman shift dependence of the scanning time to cause photodamage in myelin sheath. (a) E-CARS spectrum of a single-axonal myelin sheath measured by manually tuning the Stokes laser wavelength. The spectrum is adapted from a previous paper.¹² The peak at 2840 cm^{-1} is from the symmetric CH_2 stretch vibration. (b) Average point-scanning time needed to induce photodamage versus the Raman shift. The repetition rate is 1.3 MHz . Pump beam, 14225 cm^{-1} ; pulse peak power, 338 W ; average power, 1.10 mW . The Stokes beam frequency is tuned to generate different Raman shifts. Stokes pulse peak power, 202 W ; average power, 0.66 mW . The error bar represents the standard deviation from 10 independent measurements. Int., intensity.

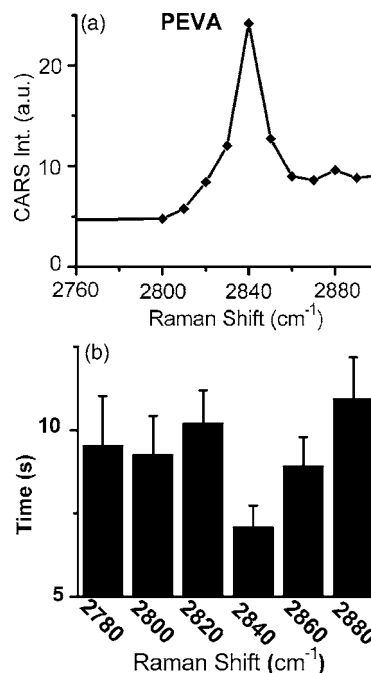


Fig. 3. Raman shift dependence of the point-scanning time for causing photodamage in a PEVA [poly(ethyl-co-vinyl acetate)] film. (a) F-CARS spectrum of a film of PEVA (40 wt. % vinyl acetate) adapted from a recent paper.¹⁵ (b) Average point-scanning time needed to induce photodamage versus the Raman shift for PEVA. The repetition rate is 3.9 MHz . Pump beam, 14268 cm^{-1} ; pulse peak power, 406 W ; average power, 3.96 mW . The Stokes beam frequency is tuned to generate different Raman shifts. Stokes pulse peak power, 101 W ; average power, 0.98 mW . The error bar represents the standard deviation from 10 independent measurements.

photon absorption.^{16,17} Similar myelin damage was also observed by using a single laser beam. Moreover, the average point-scanning time needed to cause the damage decreased with laser wavelength in the region of 700 to 900 nm . With the pump laser at 703 nm alone, the photodamage time was $2.10\pm 0.50\text{ s}$. In the Stokes wavelength range ($845\text{--}890\text{ nm}$), no photodamage was observed with the Stokes laser alone even after point scanning for minutes. Thus, the increased photodamage at 2840 cm^{-1} , which corresponds to a pump wavelength at 703 nm and a Stokes wavelength at 878 nm , was due to the Raman resonance but not to variation of the Stokes laser wavelength. A two-tailed t -test of our 2840 and 2600 cm^{-1} data was carried out to quantitatively validate the enhancement of damage. The result showed $P=0.00015$, which means that the photodamage time between two data sets had a significant difference.

A uniform polymer film sample was tested to further confirm the existence of Raman-enhanced photodamage. The photodamage experiments were performed with F-CARS from a film of poly(ethyl-co-vinyl acetate) (PEVA, 40 wt. % vinyl acetate). PEVA was first dissolved in chloroform at a concentration of 150 to 200 mg/mL . The solution was then spin coated on a cleaned coverslip. After that, films were dried under the vacuum overnight to remove the residual solvent. The final sample was a PEVA film coated on a no. 1.5 coverslip, with a thickness of around $10\text{ }\mu\text{m}$. The film was transparent for

400–1000 nm light. The F-CARS spectrum of the film is shown in Fig. 3(a). PEVA showed the strongest CARS signal at the CH₂ peak of 2840 cm⁻¹. For the photodamage experiment, we have maintained the pulse duration and the spatial and temporal overlap of the two excitation lasers during different measurements. Moreover, we controlled the laser focus to be 5 μm inside the film from the film–glass interface. The experimental results are displayed in Fig. 3(b). The data showed smaller relative standard deviations than the myelin sheath data because the polymer film sample was much more uniform. We observed that the shortest photodamage time was 7.1±0.7 s at 2840 cm⁻¹, while at other Raman shifts the average time was close to 10 s. For instance, the photodamage time at 3000 cm⁻¹ was 10.3±1.5 s. We also noticed that the difference between the on-resonance and the off-resonance photodamage time was smaller than in the spinal tissue sample. This is possibly due to a weaker CH₂ resonance enhancement in PEVA because the CARS spectrum of PEVA showed a smaller peak-to-background ratio than that of the spectrum of myelin sheath. Control experiments were conducted on the same sample with single laser beams. With the pump laser at 701 nm alone, the photodamage time was 14±1 s, while no photodamage was observed with the Stokes laser alone in the 870–887 nm range. Taken together, our CARS experiments with the polymer film and the spinal white matter showed that Raman resonance-enhanced photodamage could be a general phenomenon for solid samples that have a high density of molecular oscillators.

3. THEORETICAL ANALYSIS

To interpret the observed Raman resonance-enhanced photodamage, we now analyze the efficiencies of light–matter energy transfer in CARS microscopy in the absence and presence of Raman resonance. We consider picosecond pulses, which are used in our setup and shown to provide a high signal-to-background ratio in CARS microscopy.³² Because the pulse spatial width (0.6 mm for 2 ps pulse) is much longer than the axial length of the focus, the time-dependent field envelope is negligible. The complex representation for a linearly polarized optical field at frequency ω can be written as

$$E(t, \vec{r}) = \frac{1}{2}(\tilde{E}(\vec{r})e^{-i\omega t} + \text{c.c.}). \quad (1)$$

With this convention, the intensity flow of light in SI units can be written as $I = (\epsilon_0 c n / 2) |\tilde{E}|^2$, where c is the light speed, n is the refractive index, and ϵ_0 is the vacuum dielectric constant. Without free charges and currents, the general wave equation is^{21,33}

$$-\nabla^2 \tilde{E}(\vec{r}) = (\omega^2/c^2) \tilde{E}(\vec{r}) + \omega^2 \mu_0 P(\vec{r}), \quad (2)$$

where $P(\vec{r})$ is the polarization that contains a linear and a nonlinear component,

$$P(\vec{r}) = \epsilon_0 \chi^{(1)} \tilde{E}(\vec{r}) + P^{(3)}(\vec{r}). \quad (3)$$

In Eq. (3), $\chi^{(1)} = n^2 - 1$, with n being the refractive index. Here we have neglected $P^{(2)}$, which is 0 for centrosymmet-

ric materials. For a field propagating along the z direction, we define

$$\tilde{E}(\vec{r}) = E(\vec{r})e^{ikz}, \quad (4)$$

where $k = n\omega/c$. Substituting Eqs. (3) and (4) into Eq. (2), we have

$$\begin{aligned} & \left(k^2 E - 2ik \frac{\partial E}{\partial z} - \frac{\partial^2 E}{\partial z^2} \right) e^{ikz} - \left(\frac{\partial^2 E}{\partial x^2} + \frac{\partial^2 E}{\partial y^2} \right) e^{ikz} \\ & = k^2 E e^{ikz} + \omega^2 \mu_0 P^{(3)}. \end{aligned} \quad (5)$$

Note that E and $P^{(3)}$ are both functions of \vec{r} . Equation (5) can be recast as

$$\frac{\partial E}{\partial z} = \frac{i\omega}{2cn} P^{(3)} e^{-ikz} + \frac{i}{2k} \left(\frac{\partial^2 E}{\partial x^2} + \frac{\partial^2 E}{\partial y^2} + \frac{\partial^2 E}{\partial z^2} \right). \quad (6)$$

Equation (6) shows that $\partial E/\partial z$ is determined by two terms. The first term is the perturbation from the nonlinear polarization that accounts for the light–matter energy transfer. The second term represents the effect of field propagation.

In CARS microscopy we consider two incident fields, denoted as $E_1(\omega_1)$ and $E_2(\omega_2)$ with $\omega_1 > \omega_2$. Note that $P^{(3)}$ has different forms according to different nonlinear processes. As an example, for the CARS field (E_{as}), $P_{cars}^{(3)} \times (\omega_{as}) = (3/4) \chi_{cars}^{(3)} E_1^2 E_1^* e^{i(2k_1 - k_2)z}$ represents the nonlinear polarization at frequency ω_{as} generated by CARS, where the factor 3 is the degeneracy and the factor (1/4) comes from the convention we used in Eq. (1). The third-order susceptibility $\chi^{(3)}$ consists of a nonresonant and a resonant component. The nonresonant component $\chi_{nr}^{(3)}$ is real and positive when the excitation is far from electronic resonance.²² The resonant susceptibility $\chi_r^{(3)}$ for CARS, CSRS, SRG, and SRL has the following relationship²¹:

$$\chi_{r,cars}^{(3)} = \chi_{r,csrs}^{(3)*} = 2\chi_{r,srl}^{(3)} = 2\chi_{r,srg}^{(3)*} = \chi_r^{(3)}. \quad (7)$$

For a single Raman band the resonant susceptibility can be written as³⁴

$$\chi_r^{(3)} = \frac{NA}{\delta - i\Gamma}, \quad (8)$$

where A represents the strength of the Raman band, N is the molecular population, $\delta = \Omega - (\omega_1 - \omega_2)$ is the detuning, Ω is the molecular vibration frequency, and Γ is the half-width at half-maximum of the Raman band.

Equation (6) allows us to calculate the field change due to nonlinear interactions and to derive the difference between the output and the input power. The power change represents the energy exchange between the optical fields and the sample. Before calculating the energy transfer in CARS microscopy with tightly focused fields, we first present the analytical results for plane-wave excitations (see Appendix A for details). Under the nondepletion approximation, we have derived the following relationship at Raman resonance ($\delta = 0$):

$$\frac{\Delta I_{total}(L)}{I_{total}(0)} = \frac{\omega_1 - \omega_2}{c} \frac{I_{10} I_{20}}{I_{10} + I_{20}} \left[\frac{\omega_{as} n_2}{c n_{as}} \kappa^2 I_{10} L^2 - \frac{\omega_s n_1}{c n_s} \kappa^2 I_{20} L^2 - 2\kappa L \right]. \quad (9)$$

Here we have defined $\kappa = (3/4\epsilon_0 c n_1 n_2)(NA/\Gamma)$; L is the interaction length and I_{10} and I_{20} are the incident intensities of E_1 and E_2 , respectively. In Eq. (9), the first term is from CARS and is positive. The second term is from CSRS and is negative. The last negative term is the combined contribution of SRG and SRL. Therefore, at Raman resonance, the CARS process draws energy from the medium, while the medium absorbs energy through CSRS and SRG+SRL. The dI_{total}/dz depends on $\chi_r^{(3)}$ quadratically for the homodyne CARS and CSRS processes and linearly for SRG and SRL, which are heterodyne via mixing with the excitation fields.

Equation (9) is used to estimate the energy-transfer efficiency in the coherent Raman processes. Based on our CARS imaging parameters (Appendix B), the interaction length $L = 1.3 \mu\text{m}$ is used in the calculation. The pump and Stokes pulse energies are 0.85 and 0.51 nJ, respectively, as we used in the experiments. With a pump pulse duration of 2.0 ps and a Stokes pulse duration of 3.0 ps, the incident field intensities inside the focal volume are estimated to be $I_{10} = 0.42 \text{ TW/cm}^2$ and $I_{20} = 0.16 \text{ TW/cm}^2$. To estimate the value of NA/Γ for the CH_2 stretch vibration band in our myelin sheath sample, we use $\chi_{nr}^{(3)} = 1.4 \times 10^{-14} \text{ cm}^3/\text{erg}$ (Gaussian units, $1 \text{ cm}^3/\text{erg} = 1.4 \times 10^{-8} \text{ m}^2/\text{V}^2$) measured from the tetrahydrofuran solvent.³⁵ Based on the signal-to-background ratio of 20:1 for the CH_2 vibration band in myelin sheath,¹² we set the $\chi_r^{(3)}$ value to be $\sqrt{20} \times 1.4 \times 10^{-14} \text{ cm}^3/\text{erg} = 6.26 \times 10^{-14} \text{ cm}^3/\text{erg}$. Using the above parameters, we obtain

$$\frac{\Delta I_{total}(L)}{I_{total}(0)} = 3.37 \times 10^{-6} - 6.40 \times 10^{-7} - 7.54 \times 10^{-4} \approx -7.54 \times 10^{-4}. \quad (10)$$

Equation (10) shows that the light-matter energy transfer in coherent Raman processes in our CARS microscopy experiment is dominated by SRG and SRL. In total about 0.08% of the laser power is absorbed by the medium. The contributions from CARS and CSRS are 3 orders of magnitude smaller. Note that the above results were derived under the nondepletion assumption for the excitation fields. If the nonlinear interactions are strong enough to perturb the excitation fields, the energy transfer in CARS and CSRS is not necessarily much weaker than that in SRG and SRL. It is important to note that the coherent Raman-induced energy absorption is in the form of vibrational excitation.²¹

In nonlinear optical microscopy the beams are usually tightly focused by a high N.A. objective. Description of a tightly focused beam needs a complicated profile consisting of the fundamental Gaussian mode and other higher-order modes. While it is difficult to derive an analytical solution, we have performed numerical calculations of SRG- and SRL-induced absorption. Neglecting the pertur-

bation from nonlinear interactions, the tightly focused excitation field can be calculated by^{36,37}

$$E_x(\rho, \phi, z) = \frac{ikf \exp(-ikf)}{2} (I_{00} + I_{02} \cos 2\phi), \quad (11a)$$

$$I_{0m} = \int_0^{\alpha_{\max}} E_{inc}(\alpha) \sin \alpha \sqrt{\cos \alpha} g_m(\alpha) J_m \times (k\rho \sin \alpha) \exp(ikz \cos \alpha) d\alpha, \quad (11b)$$

$$E_{inc}(\alpha) = E_0 \exp(-f^2 \sin^2 \alpha / w_0^2), \quad (11c)$$

where ρ and ϕ are polar coordinates, f is the distance from the focal center to the edge of the lens, α_{\max} is the cone angle of the focused beam, and $N.A. = n \sin \alpha_{\max}$. Here w_0 is the radius of the incident Gaussian beam; $g_m(\alpha)$ is $(1 - \cos \alpha)$, $\sin \alpha$ or $(1 + \cos \alpha)$ when $m = 0, 1$, or 2 ; and J_m is the m th Bessel function. From the pump and Stokes fields we can calculate the induced polarization of SRG and SRL as

$$P^{(3)}(\omega_1) = 6(\chi_{nr}^{(3)} + \chi_{r,srl}^{(3)}) |E_2|^2 E_1 e^{ik_1 z}, \quad (12a)$$

$$P^{(3)}(\omega_2) = 6(\chi_{nr}^{(3)} + \chi_{r,srg}^{(3)}) |E_1|^2 E_2 e^{ik_2 z}. \quad (12b)$$

The resonant susceptibilities of Eq. (12) can be calculated using Eqs. (7) and (8).

Next, choosing an area of interest from $-z_0$ to $+z_0$, where z_0 is much bigger than the focal length, the output electric field can be calculated as

$$E(r, \phi, z_0) = E(r, \phi, -z_0) + \int_{-z_0}^{z_0} \frac{\partial E}{\partial z}(r, \phi, z) dz, \quad (13)$$

where $E(r, \phi, -z_0)$ is the input fields and $\partial E/\partial z$ in Eq. (13) can be calculated from Eq. (6). The first term on the right side of Eq. (6) represents SRG or SRL effects and can be calculated from Eq. (12). The second term represents the field propagation along the z direction and can be calculated from Eq. (11). Therefore we can calculate $\partial E_1/\partial z$ and

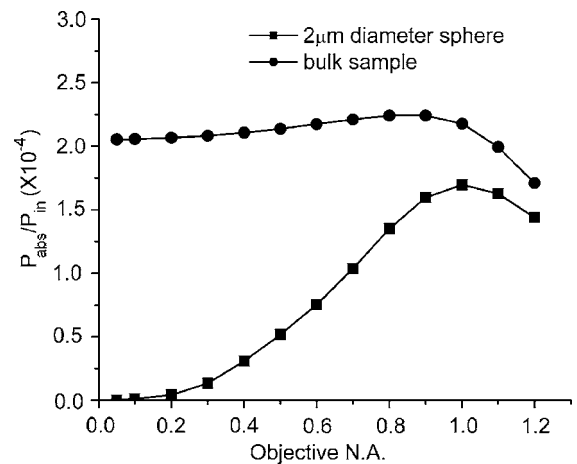


Fig. 4. Calculated power absorption percentage versus N.A. of the focusing lens for a bulk sample and a $2 \mu\text{m}$ diameter sphere sample. Pump laser wavelength, 703 nm, 0.85 nJ, 2.0 ps; Stokes laser wavelength, 878 nm, 0.51 nJ, 3.0 ps; $\chi_{nr}^{(3)} = 1.96 \times 10^{-22} \text{ m}^2/\text{V}^2$; $\chi_r^{(3)} = 8.76 \times 10^{-22} \text{ m}^2/\text{V}^2$.

$\partial E_z / \partial z$ at any point by Eq. (6). Having both the input and output fields, the integral of $I = \epsilon_0 c n |E|^2 / 2$ gives the input and output power.

In the numerical calculation, we have considered a bulk sample and a microscopic sample of a $2 \mu\text{m}$ diameter sphere placed at the focal center. We chose a $2 \mu\text{m}$ diameter because it is close to the thickness of myelin sheath in our experiments. We define the absorbed power $P_{abs} = -\Delta P_{total}$. For each sample we calculated the power absorption ratio (P_{abs}/P_{in}) as a function of the N.A. of the focusing lens. The results are shown in Fig. 4. For the $2 \mu\text{m}$ sphere sample, the absorption is negligible with weakly focused beams but it quickly increases with the N.A. A maximum is seen at N.A. = 1.0. When N.A. exceeds 1.0, the axial FWHM of focal volume $2n\lambda / (\text{N.A.})^2$ of the pump beam becomes smaller than the diameter of the sphere ($2 \mu\text{m}$). At N.A. = 1.2, P_{abs}/P_{in} was calculated to be 1.4×10^{-4} . For the bulk sample the absorption appears to be insensitive to N.A. because the low field intensity at smaller N.A. is partially compensated by the longer interaction length.

4. MECHANISMS FOR COHERENT RAMAN-ENHANCED PHOTODAMAGE

To understand the role of Raman-induced absorption in the photodamage process, we need to take a close look at the photodamage mechanism. Based on our observations in Fig. 1, we consider the photodamage to myelin to be plasma-induced photodisruption.³⁰ For this kind of damage, free electrons are generated by UV or multiphoton absorption and plasma is consequently formed. The resultant plasma strongly absorbs the light and spreads into the surrounding tissues, generating shockwaves [Figs. 1(c)–1(e) in Ref. 19] and cavitation [Fig. 1(b)]. Although the coherent Raman-induced vibrational absorption does not heat electrons directly, the vibrational excitation can assist electron heating by superelastic collision, as shown in the gas phase.^{38,39} We note that the first excited vibrational level in general has lower energy than excited electronic levels. Nevertheless, high-quantum vibrational levels can be excited through two possible ways. The first is vibration–vibration energy exchange upon molecular collision,⁴⁰ which increases the vibrational level of one molecule at the cost of another molecule's vibrational energy. This pathway is possible for lipid membranes, which are known to be modeled as a two-dimensional fluid.⁴¹ The second is the overtone vibrational excitation by stimulated Raman pumping.⁴² As a result, the absorbed vibrational energy can be transferred to the electronic system, resulting in the enhanced photodamage as we observed.

We note that three kinds of absorption coexist in our experiments: linear absorption, Raman-induced vibrational absorption, and multiphoton electronic absorption. The importance of Raman-induced absorption depends on its relative strength compared with the other two absorption processes. Taking myelin sheath as an example, the linear absorption coefficient of brain white matter (also rich in myelinated axons) at our laser wavelength was shown to be 0.5 cm^{-1} .⁴³ Thus, the power absorption ratio (P_{abs}/P_{in}) is 0.5×10^{-4} over $1 \mu\text{m}$ (the axial length of the

focus), about three times smaller than Raman-induced absorption. The exact two-photon absorption cross section of myelin sheath is unknown. Here we assume a typical value of $\sim 10^{-50} \text{ cm}^4 \text{ s photon}^{-1} \text{ molecule}^{-1}$.⁴⁴ In our experiments the maximum laser intensity of the pump beam at focal center is $1.5 \times 10^{30} \text{ photon cm}^{-2} \text{ s}^{-1}$, calculated from $I_{10} = 0.42 \text{ TW/cm}^2$ used for Eq. (10) and the photon energy of $2.85 \times 10^{-19} \text{ J}$ at the wavelength of 700 nm. For a lipid membrane sample, the area of a lipid molecule is about 0.7 nm^2 , the thickness of a monolayer is about 2.5 nm ,⁴⁵ and the lipid concentration is $6 \times 10^{20} \text{ molecule cm}^{-3}$. Under these conditions, the two-photon absorption coefficient is estimated to be 9 cm^1 at the focal center, which results in a power absorption ratio (P_{abs}/P_{in}) of 9×10^{-4} . This value is of the same order of magnitude as Raman-induced absorption. The above estimated values interpret our results in Fig. 2(b) well. At the off-resonance Raman shifts, there is no Raman-induced absorption. In such cases, two-photon absorption could account for the photodisruption of myelin. At 2840 cm^{-1} , the Raman-induced absorption provided additional electron heating. Moreover, the contribution from the coherent Raman processes is comparable to that from two-photon absorption. As a result, for myelin sheath the point-scanning time to induce the damage is reduced by half at the Raman resonance [Fig. 2(b)].

It was shown by Banin *et al.* that multiphoton ionization requires less laser intensity than Raman pumping when femtosecond lasers in the visible wavelength region are used.⁴⁶ It is important to point out that multiphoton absorption–induced ionization can be diminished in CARS microscopy owing to the use of near-infrared picosecond pulses. By using a 2.5 ps laser pulse, for which the spectral width matches the linewidth of CH_2 stretch vibration, the laser energy can be effectively concentrated on Raman resonance rather than broadband electronic transition. Moreover, vibrational pumping can occur even in the absence of electronic resonance. As a result, Raman resonance-enhanced photodamage of the myelin sheath and the polymer film sample was observed as shown in Figs. 2 and 3.

In the above calculations the laser peak power was close to 500 W at the sample. If we lower the laser peak power by 10 times, both Raman-induced absorption and two-photon absorption will be reduced by 10 times as well. In such a case, linear absorption could start to play a dominant role. This is what we observed in Figs. 3 and Fig. 4(b) of Ref. 19, where lower peak power (below 80 W) and higher repetition rate (~ 14 – 15.6 MHz) were used. In Fig. 3 of Ref. 19, the relationship between photodamage rate and laser peak power became less than quadratic at the peak power of 74 W. In Fig. 4(b) of Ref. 19, photodamage no longer appeared to be enhanced by Raman-induced absorption at the peak power of 32 W, probably because at this peak power linear absorption dominated the photodamage process.

Based on the above discussion, the peak power of the picosecond lasers used in our CARS microscope lies in the region where both linear and nonlinear absorption can make important contributions to photodamage. With a femtosecond laser source usually used in two-photon fluorescence imaging, two-photon absorption and higher-

order processes are expected to dominate the photodamage process.¹⁶

5. CONCLUSIONS

In CARS microscopy study of spinal tissues and PEVA films, the point-scan time for induction of photodamage was reduced by 50% and 30%, respectively, when the excitation was tuned from off resonance to on resonance with the CH₂ stretch vibration. An assessment of light-matter energy exchange was carried out to interpret the observed Raman resonance-enhanced photodamage. The light-matter energy transfer was analyzed for the CARS, CSRS, SRG, and SRL processes that simultaneously occur in CARS microscopy. At Raman resonance, the CARS and SRL processes transfer energy from the material to the optical fields, while the CSRS and SRG processes induce vibrational absorption in the material. The dominant energy exchange is material absorption induced by the heterodyne SRG and SRL processes. With a peak laser power of ~500 W at the sample, Raman-induced vibrational absorption is about 1.4×10^{-4} of the incident power by assuming a 2 μm diameter spherical sample at the focal center. It is at the same order of magnitude as the two-photon absorption and could contribute to additional electron heating. As a result, the photodamage is enhanced when the excitation beams are tuned to Raman resonance.

APPENDIX A

In the case of plane-wave fields, the derivatives with respect to x, y , and z are 0 in Eq. (6). In CARS microscopy we consider the two incident fields $E_1(\omega_1)$ and $E_2(\omega_2)$ and the two new fields (E_{as} and E_s) generated by CARS and CSRS. The phase-matching condition is automatically satisfied for SRG and SRL, and we assume that it is also satisfied for CARS and CSRS. This assumption is valid for microscopy in which the light-sample interaction length is a few micrometers or even shorter.³⁷ From Eq. (6), the coupling equations among the four fields can be written as

$$\frac{\partial E_{as}}{\partial z} = \frac{i\omega_{as}}{8cn_{as}} 3(\chi_{nr}^{(3)} + \chi_{r,cars}^{(3)})E_1^2E_2^*, \quad (\text{A1a})$$

$$\frac{\partial E_s}{\partial z} = \frac{i\omega_s}{8cn_s} 3(\chi_{nr}^{(3)} + \chi_{r,csrs}^{(3)})E_2^2E_1^*, \quad (\text{A1b})$$

$$\begin{aligned} \frac{\partial E_1}{\partial z} = & \frac{i\omega_1}{8cn_1} [(6\chi_{nr}^{(3)} + 3\chi_{r,cars}^{(3)*})E_1^*E_2E_{as} \\ & + 3\chi_{nr}^{(3)}E_2^2E_s^* + 6(\chi_{nr}^{(3)} + \chi_{r,srl}^{(3)})|E_2|^2E_1], \end{aligned} \quad (\text{A1c})$$

$$\begin{aligned} \frac{\partial E_2}{\partial z} = & \frac{i\omega_2}{8cn_2} [3\chi_{nr}^{(3)}E_1^2E_{as}^* + (6\chi_{nr}^{(3)} \\ & + 3\chi_{r,csrs}^{(3)*})E_1E_2^*E_s \\ & + 6(\chi_{nr}^{(3)} + \chi_{r,sg}^{(3)})|E_1|^2E_2]. \end{aligned} \quad (\text{A1d})$$

Here, n_1, n_2, n_{as} , and n_s denote the refractive index of the material at frequencies $\omega_1, \omega_2, \omega_{as}$, and ω_s , respectively. The factors 3 and 6 before $\chi^{(3)}$ are the degeneracy.

We now derive the change of total field energy ($I_{total} = I_1 + I_2 + I_{as} + I_s$) during the propagation, dI_{total}/dz . If dI_{total}/dz is positive, the light fields draw energy from the material; if it is negative, the material absorbs energy from the light. To derive dI_{total}/dz , we first calculate dI/dz for each of the four interacting waves by using the following equation:

$$\frac{dI_m}{dz} = \epsilon_0 cn_m \cdot \text{Re} \left(E_m^* \frac{dE_m}{dz} \right), \quad (\text{A2})$$

where $m = 1, 2, s$, or as . Substituting Eqs. (A1a)–(A1d) and $\chi_r^{(3)}$, defined in Eq. (7), into Eq. (A2) we obtain

$$\frac{dI_{as}}{dz} = - \frac{3\epsilon_0\omega_{as}}{8} [\text{Im}(\chi_{nr}^{(3)}E_1^2E_2^*E_{as}^*) + \text{Im}(\chi_r^{(3)}E_1^2E_2^*E_{as}^*)], \quad (\text{A3a})$$

$$\frac{dI_s}{dz} = - \frac{3\epsilon_0\omega_s}{8} [\text{Im}(\chi_{nr}^{(3)}E_1^*E_2^2E_s^*) + \text{Im}(\chi_r^{(3)*}E_1^*E_2^2E_s^*)], \quad (\text{A3b})$$

$$\begin{aligned} \frac{dI_1}{dz} = & - \frac{3\epsilon_0\omega_1}{8} [-2 \text{Im}(\chi_{nr}^{(3)}E_1^2E_2^*E_{as}^*) - \text{Im}(\chi_r^{(3)}E_1^2E_2^*E_{as}^*) \\ & + \text{Im}(\chi_{nr}^{(3)}E_1^*E_2^2E_s^*) + \text{Im}(\chi_r^{(3)}|E_1|^2|E_2|^2)], \end{aligned} \quad (\text{A3c})$$

$$\begin{aligned} \frac{dI_2}{dz} = & - \frac{3\epsilon_0\omega_2}{8} [-2 \text{Im}(\chi_{nr}^{(3)}E_1^*E_2^2E_s^*) - \text{Im}(\chi_r^{(3)*}E_1^*E_2^2E_s^*) \\ & + \text{Im}(\chi_{nr}^{(3)}E_1^2E_2^*E_{as}^*) - \text{Im}(\chi_r^{(3)}|E_1|^2|E_2|^2)]. \end{aligned} \quad (\text{A3d})$$

To calculate the total field-energy change, we add up Eqs. (A3a)–(A3d). According to the relationship $\omega_{as} - \omega_1 = \omega_1 - \omega_2 = \omega_2 - \omega_s$, the nonresonant terms cancel each other. Thus we have

$$\begin{aligned} \frac{dI_{total}}{dz} = & - \frac{3\epsilon_0(\omega_1 - \omega_2)}{8} [\text{Im}(\chi_r^{(3)}E_1^2E_2^*E_{as}^*) - \text{Im}(\chi_r^{(3)*}E_1^*E_2^2E_s^*) \\ & + \text{Im}(\chi_r^{(3)}|E_1|^2|E_2|^2)]. \end{aligned} \quad (\text{A4})$$

The first and second terms in Eq. (A4) represent the field-energy change induced by CARS and CSRS, respectively. The third term represents the field-energy change by the SRG and SRL processes. In the absence of Raman resonance, $\chi_r^{(3)}$ is 0, and thus no light-matter energy transfer occurs.

To simplify the calculations for E_{as} and E_s in Eq. (A4), we use the nondepletion approximation for E_1 and E_2 ; i.e., the light-matter interactions have low efficiency and thus induce very little change in the excitation fields.⁴⁷ This assumption is reasonable for coherent Raman processes, which have low conversion efficiencies. By assuming that the medium starts from $z = 0$, we integrate Eqs. (A1a) and (A1b) to obtain the amplitude for E_{as} and E_s ,

$$E_{as}(z) = \frac{i\omega_{as}}{8cn_{as}} 3(\chi_{nr}^{(3)} + \chi_r^{(3)}) E_1^2 E_2^* z, \quad (\text{A5a})$$

$$E_s(z) = \frac{i\omega_s}{8cn_{as}} 3(\chi_{nr}^{(3)} + \chi_r^{(3)*}) E_2^2 E_1^* z. \quad (\text{A5b})$$

The excitation fields E_1 and E_2 are related to the energy by

$$|E_m|^2 = \frac{2I_m}{\epsilon_0 cn_m}, \quad (\text{A6})$$

where $m=1$ or 2 . Substituting Eqs. (A5) and (A6) into Eq. (A4), we have

$$\begin{aligned} \frac{dI_{total}}{dz} = \frac{\omega_1 - \omega_2}{c} & \left[\frac{9\omega_{as}}{8\epsilon_0^2 c^3 n_1^2 n_2 n_{as}} (\chi_{nr}^{(3)} \text{Re}(\chi_r^{(3)}) + |\chi_r^{(3)}|^2) I_1^2 I_2 z \right. \\ & - \frac{9\omega_s}{8\epsilon_0^2 c^3 n_1 n_2^2 n_s} (\chi_{nr}^{(3)} \text{Re}(\chi_r^{(3)}) + |\chi_r^{(3)}|^2) I_1 I_2^2 z \\ & \left. - \frac{3}{2\epsilon_0 cn_1 n_2} \text{Im}(\chi_r^{(3)}) I_1 I_2 \right]. \quad (\text{A7}) \end{aligned}$$

Similar to Eq. (A4), the first, second, and third terms in Eq. (A7) arise from CARS, CSRS, and SRG+SRL, respectively. At Raman resonance ($\delta=0$), $\chi_r^{(3)}$ equals iNA/T . Equation (A7) becomes

$$\begin{aligned} \frac{dI_{total}}{dz} = \frac{\omega_1 - \omega_2}{c} & \left[\frac{9\omega_{as}}{8\epsilon_0^2 c^3 n_1^2 n_2 n_{as}} \left(\frac{NA}{\Gamma} \right)^2 I_1^2 I_2 z \right. \\ & \left. - \frac{9\omega_s}{8\epsilon_0^2 c^3 n_1 n_2^2 n_s} \left(\frac{NA}{\Gamma} \right)^2 I_1 I_2^2 z - \frac{3}{2\epsilon_0 cn_1 n_2} \frac{NA}{\Gamma} I_1 I_2 \right]. \quad (\text{A8}) \end{aligned}$$

To derive the percentage of the energy transfer over the interaction length L , we integrate Eq. (A8) from $z=0$ to L . Following the nondepletion approximation, we use the incident-field intensities I_{10} and I_{20} instead of I_1 and I_2 during the integration. Then we divide the integral by $I_{total}(0) = I_{10} + I_{20}$. The result is

$$\begin{aligned} \frac{\Delta I_{total}(L)}{I_{total}(0)} = \frac{\omega_1 - \omega_2}{c} \frac{I_{10} I_{20}}{I_{10} + I_{20}} & \left[\frac{\omega_{as} n_2}{c n_{as}} \kappa^2 I_{10} L^2 \right. \\ & \left. - \frac{\omega_s n_1}{c n_s} \kappa^2 I_{20} L^2 - 2\kappa L \right]. \quad (\text{A9}) \end{aligned}$$

This is Eq. (9) in the main text.

APPENDIX B

In our CARS imaging experiment, the pump and Stokes beam frequencies are set as $\omega_1/c = 2\pi \times 14225 \text{ cm}^{-1}$ and $\omega_2/c = 2\pi \times 11385 \text{ cm}^{-1}$,¹² respectively. The corresponding wavelengths are 703 and 878 nm, respectively. All refractive indices are chosen to be $n = 1.33$ (index for water). A $60\times$ water-immersion objective (N.A.=1.2) was used in our experiments. It is well known that the lateral and axial FWHM of the focal volume can be calculated by $0.61\lambda/\text{N.A.}$ and $2n\lambda/(\text{N.A.})^2$, respectively. For the pump

beam they are calculated to be 0.36 and 1.30 μm , and for the Stokes beam they are 0.45 and 1.62 μm , respectively. Therefore $L = 1.3 \mu\text{m}$ is used in the calculation to derive Eq. (10).

ACKNOWLEDGMENTS

This work is supported by NSF grant 0416785 and NIH R21 grant EB004966-01. The authors thank Riyi Shi for providing the spinal tissue sample and Eunah Kang in Kinam Park's group for providing the polymer film sample.

All correspondence should be addressed to J.-X. Cheng at jcheng@purdue.edu.

REFERENCES

1. J. X. Cheng and X. S. Xie, "Coherent anti-Stokes Raman scattering microscopy: instrumentation, theory, and applications," *J. Phys. Chem. B* **108**, 827–840 (2004).
2. A. Zumbusch, G. R. Holtom, and X. S. Xie, "Three-dimensional vibrational imaging by coherent anti-Stokes Raman scattering," *Phys. Rev. Lett.* **82**, 4142–4145 (1999).
3. N. Dudovich and Y. Silberberg, "Single-pulse coherently controlled nonlinear Raman spectroscopy and microscopy," *Nature* **418**, 512–514 (2002).
4. T. Ichimura, N. Hayazawa, M. Hashimoto, Y. Inouye, and S. Kawata, "Tip-enhanced coherent anti-Stokes Raman scattering for vibrational nanoimaging," *Phys. Rev. Lett.* **92**, 220801 (2004).
5. T. W. Kee and M. T. Cicerone, "Simple approach to one-laser, broadband coherent anti-Stokes Raman scattering microscopy," *Opt. Lett.* **29**, 2701–2703 (2004).
6. T.-W. Koo, S. Chan, and A. A. Berlin, "Single-molecule detection of biomolecules by surface-enhanced coherent anti-Stokes Raman scattering," *Opt. Lett.* **30**, 1024–1026 (2005).
7. D. L. Marks and S. A. Boppart, "Nonlinear interferometric vibrational imaging," *Phys. Rev. Lett.* **92**, 123905 (2004).
8. V. V. Yakovlev, "Advanced instrumentation for non-linear Raman microscopy," *J. Raman Spectrosc.* **34**, 957–964 (2003).
9. L. Li, H. Wang, and J. X. Cheng, "Quantitative coherent anti-Stokes Raman scattering imaging of lipid distribution in co-existing domains," *Biophys. J.* **89**, 3480–3490 (2005).
10. E. O. Potma and X. S. Xie, "Direct visualization of lipid phase segregation in single lipid bilayers with coherent anti-Stokes Raman scattering microscopy," *ChemPhysChem* **6**, 77–79 (2005).
11. G. W. H. Wurpel, H. A. Rinia, and M. Müller, "Imaging orientational order and lipid density in multilamellar vesicles with multiplex CARS microscopy," *J. Microsc.* **218**, 37–45 (2005).
12. H. Wang, Y. Fu, P. Zickmund, R. Shi, and J. X. Cheng, "Coherent anti-Stokes Raman scattering imaging of live spinal tissues," *Biophys. J.* **89**, 581–591 (2005).
13. C. L. Evans, E. O. Potma, M. Puoris'haag, D. Côté, C. P. Lin, and X. S. Xie, "Chemical imaging of tissue *in vivo* with video-rate coherent anti-Stokes Raman scattering microscopy," *Proc. Natl. Acad. Sci. U.S.A.* **102**, 16807–16812 (2005).
14. X. Nan, J. X. Cheng, and X. S. Xie, "Vibrational imaging of lipid droplets in live fibroblast cells using coherent anti-Stokes Raman microscopy," *J. Lipid Res.* **40**, 2202–2208 (2003).
15. E. Kang, H. Wang, I. K. Kwon, J. Robinson, K. Park, and J. X. Cheng, "*In situ* visualization of paclitaxel distribution and release by coherent anti-Stokes Raman scattering microscopy," *Anal. Chem.* **78**, 8036–8043 (2006).
16. A. Hopt and E. Neher, "Highly nonlinear photodamage in

- two-photon fluorescence microscopy," *Biophys. J.* **80**, 2029–2036 (2001).
17. K. König, T. W. Becker, P. Fischer, I. Riemann, and K.-J. Halbhuber, "Pulse-length dependence of cellular response to intense near-infrared laser pulses in multiphoton microscopes," *Opt. Lett.* **24**, 113–115 (1999).
 18. A. Vogel, J. Noack, G. Huettmann, and G. Paltauf, "Femtosecond-laser-produced low-density plasmas in transparent biological media: a tool for the creation of chemical, thermal, and thermomechanical effects below the optical breakdown threshold," *Proc. SPIE* **4633A**, 1–15 (2002).
 19. Y. Fu, H. Wang, R. Shi, and J. X. Cheng, "Characterization of photodamage in coherent anti-Stokes Raman scattering microscopy," *Opt. Express* **14**, 3942–3951 (2006).
 20. R. J. H. Clark and R. E. Hester, *Advances in Non-Linear Spectroscopy* (Wiley, 1988), Vol. 15.
 21. J. S. Gomez, "Coherent Raman spectroscopy," in *Modern Techniques in Raman Spectroscopy*, J. J. Laserna, ed. (Wiley, 1996), pp. 309–342.
 22. Y. R. Shen, *The Principle of Non-Linear Optics* (Wiley, 1984).
 23. S. A. Akhmanov, "Coherent active spectroscopy of combinatorial (Raman) scattering with tunable oscillators: comparison with the spontaneous scattering technique," in *Nonlinear Spectroscopy*, N. Bloembergen, ed. (North-Holland, 1977), pp. 217–254.
 24. G. L. Eesley, *Coherent Raman Spectroscopy* (Pergamon, 1981).
 25. R. W. Hellwarth, "Third order nonlinear susceptibility of liquids and solids," *Prog. Quantum Electron.* **5**, 1–68 (1977).
 26. M. D. Levenson and J. J. Song, "Coherent Raman spectroscopy," in *Coherent Nonlinear Optics (Topics in Current Physics 21)*, M. S. Feld and V. S. Letokhov, eds. (Springer-Verlag, 1980), pp. 293–373.
 27. P. N. Butcher and D. Cotter, *The Elements of Nonlinear Optics* (Cambridge U. Press, 1990).
 28. C. C. Shang and H. Hsu, *IEEE J. Quantum Electron.* **QE-23**, 117–119 (1987).
 29. P. Morell and R. H. Quarles, "Myelin formation, structure, and biochemistry," in *Basic Neurochemistry: Molecular, Cellular, and Medical Aspects*, 5th ed., G. J. Siegel, B. W. Agranoff, R. W. Alberts, and P. B. Molinoff, eds. (Lippincott, 1999).
 30. P. N. Prasad, *Introduction to Biophotonics* (Wiley Interscience, 2003), pp. 168–175.
 31. J. Diels and W. Rudolph, "Generation of extreme wavelengths," in *Ultrashort Laser Pulse Phenomena: Fundamentals, Techniques, and Applications on a Femtosecond Time Scale* (Academic, 1996), pp. 472–475.
 32. J. X. Cheng, A. Volkmer, L. D. Book, and X. S. Xie, "An epi-detected coherent anti-Stokes Raman scattering (E-CARS) microscope with high spectral resolution and high sensitivity," *J. Phys. Chem. B* **105**, 1277–1280 (2001).
 33. S. Mukamel, *Principles of Nonlinear Optical Spectroscopy* (Oxford U. Press, 1995), p. 542.
 34. H. Lotem, J. R. T. Lynch, and N. Bloembergen, "Interference between Raman resonances in four-wave difference mixing," *Phys. Rev. A* **14**, 1748–1755 (1976).
 35. W. Zhao, H. Li, R. West, and J. C. Wright, "Measurement of the third-order nonlinear susceptibility in a representative soluble polymer with acetylenic linkages," *Chem. Phys. Lett.* **281**, 105–110 (1997).
 36. B. Richards and E. Wolf, "Electromagnetic diffraction in optical systems. II. Structure of the image field in an aplanatic system," *Proc. R. Soc. London Ser. A* **253**, 358–379 (1959).
 37. J. X. Cheng, A. Volkmer, and X. S. Xie, "Theoretical and experimental characterization of coherent anti-Stokes Raman scattering microscopy," *J. Opt. Soc. Am. B* **19**, 1363–1375 (2002).
 38. E. Plönjes, P. Palm, J. W. Richa, I. V. Adamovich, and W. Urban, "Electron-mediated vibration–electronic (V–E) energy transfer in optically pumped plasmas," *Chem. Phys.* **279**, 43–54 (2002).
 39. W. Lee, K. Frederickson, P. Palm, I. Adamovich, J. W. Rich, and W. Lempert, "Mitigation of oxygen attachment in high pressure air plasmas by vibrational excitation," in *35th AIAA Plasmadynamics and Lasers Conference* (AIAA, 2004), paper AIAA 2257–2004.
 40. C. E. Treanor, J. W. Rich, and R. G. Rehm, "Vibrational relaxation of anharmonic oscillators with exchange-dominated collisions," *J. Chem. Phys.* **48**, 1798–1807 (1968).
 41. S. J. Singer and G. L. Nicolson, "Fluid mosaic model of structure of cell-membranes," *Science* **175**, 720–731 (1972).
 42. K. Ravichandran, M. Yorgancioglu, and T. R. Fletcher, "A simple method for quantitative comparisons of mode specific chemistry using stimulated Raman excitation," *J. Chem. Phys.* **101**, 3406–3409 (1994).
 43. P. van der Zee, M. Essenpreis, and D. T. Delpy, "Optical properties of brain tissue," *Proc. SPIE* **1888**, 454–465 (1993).
 44. P. T. C. So, H. Kim, and I. E. Kochevar, "Two-photon deep tissue *ex vivo* imaging of mouse dermal and subcutaneous structures," *Opt. Express* **3**, 339–350 (1998).
 45. J. F. Nagle, "Area/lipid of bilayers from NMR," *Biophys. J.* **64**, 1476–1481 (1993).
 46. U. Banin, A. Bartana, S. Ruhman, and R. Kosloff, "Impulsive excitation of coherent vibrational motion ground surface dynamics induced by intense short pulses," *J. Chem. Phys.* **101**, 8461–8481 (1994).
 47. G. D. Boyd and D. A. Kleinman, "Parametric interaction of focused Gaussian light beams," *J. Appl. Phys.* **39**, 3597–3639 (1968).